Generation of dissipative solitons in a doped optical fiber modeled by the higher-order dispersive cubic-quintic-septic complex Ginzburg-Landau equation

Dieudonné Zanga,[1,*] Serge I. Fewo,[1,†] Conrad B. Tabi,[2,‡] and Timoléon C. Kofané[1,2,§]

[1]*Laboratory of Mechanics, Materials and Structures, Department of Physics, Faculty of Science, University of Yaounde I, P. O. Box 812, Yaounde, Cameroon*

[2]*Department of Physics and Astronomy, Botswana International University of Science and Technology, Private Bag 16 Palapye, Botswana*

(Received 30 March 2021; accepted 7 January 2022; published 4 February 2022)

The generation of dissipative optical solitons is explored in doped fibers with correction effects under the activation of modulational instability (MI). The model, described by the cubic-quintic-septic complex Ginzburg-Landau equation, includes higher-order dispersion and nonlinear gradient terms. The Lange-Newell's criterion for MI of Stokes wave, boundary domains of MI, and integrated gain of MI are obtained via the linear stability analysis. Particular attention is given to the physical effect on the critical frequency detuning, especially in the normal regime, when varying the values of odd dispersion coefficients. Numerical simulations are undertaken and confronted with analytical predictions. Beyond the agreement between the linear stability analysis and trains of soliton generation, the soliton map induced by MI, along with the subsequent physical effects, is debated via bifurcation diagrams. This allows accurate prediction of transitions between various types of localized modes and well-calibrated generation of a wide variety of solitons with different energies. It is argued that knowing the center of mass and the energy of the generated structures can better characterize the long-time evolution of MI and, eventually, its nonlinear manifestations.

DOI: 10.1103/PhysRevA.105.023502

I. INTRODUCTION

During the past two centuries, the concept of solitons has attracted considerable interest in theory and experiment. One of the main characteristics of solitons is that they propagate for a long time and over very long distances without visible changes. This feature makes them suitable vehicles for energy and information transport [1]. Mathematically, solitons are solutions to nonlinear partial differential equations and emerge in nonlinear systems under a balanced interaction between dispersive and nonlinear effects and additional compensation between loss and gain impacts when the system is dissipative [2–4]. Over the years, the discovery of solitons has triggered the development of several theories and applications in many physical systems ranging from hydrodynamics to optical fibers, through plasma, semiconductors, cold atoms, electrical transmission lines, and biophysics [1–5], to name a few. Putting a high point on optical communications, propagation of light has been the turning point of several research works that revealed a wide variety of solitons and their technological implications. In that direction, bright and dark solitons in Hamiltonian systems governed by the nonlinear Schrödinger equation were proposed in a seminal work by Hasegawa and his coworkers [5]. Theoretical and experimental studies of dissipative solitons dynamics, including other subsequent numerical studies, were developed by Akhmediev and his coworkers using the cubic-quintic complex Ginzburg-Landau (CQGL) equation. Importance was given to theoretical and experimental optical solitons, namely pulsating solitons, chaotic solitons, creeping solitons, exploding solitons, and, recently, auto solitons with extreme spikes [6–12]. Along the same line, Carvalho and Faâo proved the existence of dissipative solitons and further addressed their stability in the presence of nonlinear gradient and cubic nonlinearity terms [13–15] gradient and cubic nonlinearity terms [16,17].

In modern telecommunication systems, the central role of a dopant is boosting optical wave transmission in the fiber. Often called rare earths or lanthanide, dopants are found in a group of 14 similar elements, with atomic numbers ranging from 58 to 71, whose contributions and specifications have received increasing attention in the past three decades [17]. For example, ytterbium-doped fiber [18–20], thulium-doped fiber [21], and erbium-doped fiber [22–26] acquire remarkable proprieties when they are doped in silica or glass fiber as commonly exhibited by their susceptibility whose orders and combinations are of crucial importance. On that note, competing susceptibility can be noticed when silica is doped for optical fibers and in the case of semiconductors [27]. In general, beneath the action of the dopant, the order of susceptibility may increase up to 7, and the material may exhibit χ^3, χ^5, and χ^7 (cubic, quintic, and septic) susceptibilities [28,29]. It is essential to point out that such materials exhibit a saturation of the third-order nonlinear susceptibility χ^3 which is equivalent to the presence of fifth- and seventh-order nonlinear susceptibilities χ^5 and χ^7. Experimental results related to the material sample As_2S_3, which enable the measurement of the septic order

*dieudonne.zanga@yahoo.fr
†Corresponding author: sergefewo@yahoo.fr
‡tabic@biust.ac.bw
§tckofane@yahoo.com

susceptibility, are available. New research directions confirm the experimental use of the latter in boosting the propagation of ultrashort femtosecond optical pulses [28,29], which requires higher-order dispersion and nonlinearities inherent to dopants [30–39]. Optical solitons through a doped or undoped fiber find several applications, mainly in optical atomic clocks, photonic radar, coherent communications, ultrafast distance measurements, and optical frequency synthesizer [40]. A key mechanism that leads to the emergence of localized coherent nonlinear structures and trains of ultrashort pulses is modulational instability (MI). The latter occurs in optical fibers because of the interplay between nonlinear and dispersive effects. In the literature, there are two distinguishable types of MI, the one due to quantum noise (spontaneous MI) and the one originating from the frequency-shifted signal (induced MI). In general, the common signature of MI is the exponential growth of the amplitude or phase of a disturbing wave during propagation. This applies to a broad range of physics areas, including Bose-Einstein condensate [41–44], plasma physics [45–48], fluid dynamics [49,50], and biophysics [51,52], to cite a few. In nonlinear optics, it was found in metamaterials [53], nonlocal systems [54–56], fiber Bragg gratings [57–60], twin-core fiber [61], asymmetry dual-core fiber [62], microcavities [63], and doped resonant fiber [64]. Agrawal studied the modulational instability in doped optical fiber with rare earth [65]. Indeed, great interest has recently been given to higher-order nonlinear optical systems, principally because they can be used to generate ultrashort optical solitons at a very high bit rate on the one hand, and for performance improvement during trans-oceanic and transcontinental propagations, on the other hand [30–33,63,66]. We should stress that a wide variety of idealized structures, which may be either stationary, periodic, or spatiotemporal, have found their origin in the process of MI, among which are energy localization, the emergence of rogue waves, Fermi-Pasta-Ulam recurrence, nonlinear phase shift, Akhmediev breathers, Kuznetsov-Ma soliton, and the Peregrine soliton. Indeed, such structures can become chaotic. Of course, it was established, via bifurcation theory, that dissipative solitons can behave as strange attractors in low-dimensional systems [67]. Alternatively, as said so far, the same entities emerge as the consequence of MI, which intuitively brings together the two theories and calls for more investigations to find out the connection between the two concepts that, unfortunately, have always been treated separately.

It is the main objective of the present paper to study the emergence of ultrashort optical solitons in nonlinear doped fibers, which include higher-order dispersions, higher-order non-Kerr nonlinearities, as well as higher-order self-steepening and self-shifting terms. The generic model to be used is an extended CGL. Our contribution goes beyond direct confirmation of analytical prediction through direct numerical simulations to involve other useful indicators of ultrashort optical soliton generation such as the center of mass, the energy, and bifurcation diagrams. This study paves a way to studying and characterizing optical solitons that combine the standard theory of MI and the bifurcation theory, especially in a context where higher-order effects are included, therefore increasing the number of parameters of the CGL equation capable of significantly affecting the bifurcation boundaries.

The rest of the paper is therefore outlined as follows. In Sec. II, we introduce the dissipative model of propagation of ultrashort pulses, namely the cubic-quintic-septic complex Ginzburg-Landau equation with higher-order dispersion, self-steeping, and self-shifting effects associated with their correction terms. Section III is devoted to the linear stability analysis of the Stokes wave. The stability conditions and the amplitude threshold are explicitly determined. In Sec. IV, details on the MI development are given, where one discusses the variation of the boundary domains of MI frequency along with the analytical features of the gain. Numerical experiments are also undertaken in order to simulate the soliton maps induced during the propagation, along with the appropriate bifurcation diagrams and a parametric comparison between the energy and the center of mass. Section V gives some concluding remarks.

II. THEORETICAL MODEL

In this section, we consider the higher order CGL equation with non-Kerr nonlinearities terms, written as [68]

$$i\psi_\xi + \sum_{j=2}^{6} d_{jrs}\psi_{j\tau} + \gamma_{rs}\psi + \sum_{k=1}^{3}[(q_{krs}|\psi|^{2k} + m_{kr}|\psi|_\tau^{2k})\psi + in_{ks}(|\psi|^{2k}\psi)_\tau] = 0, \tag{1}$$

where $\psi(\xi,\tau)$ is a paraxial beam. The coordinate ξ is the propagation distance and τ is the retarded time in the frame moving with the pulse. All the coefficients are real constants. The complex coefficient of absorption $\gamma_{rs} = \gamma_r + i\gamma_s$, where $\gamma_r = \frac{g_p\delta}{2n(1+\delta^2)}$ is the linear gain (if positive) and $\gamma_s = -\alpha + \frac{g_p}{2n(1+\delta^2)}$ is the frequency shift coefficient. Parameters $g_p, \delta, \alpha, n,$ are peak gain, frequency difference between vibration of electric field and the vibration frequency of atoms of dopant, fiber loss coefficient, and nonlinear index, respectively. The parameter $d_{2r} = -\frac{\beta_2}{2} - \frac{g_p(-3\delta+\delta^3)T_2^2}{2n(1+\delta^2)^3}$ measures the wave dispersion, while $d_{2s} = -\frac{g_p(1-3\delta^2)T_2^2}{2n(1+\delta^2)^3}$ measures the spectral filtering. The complex coefficients $d_{3rs} = d_{3r} + id_{3s}$, $d_{4rs} = d_{4r} + id_{4s}$, $d_{5rs} = d_{5r} + id_{5s}$, and $d_{6rs} = d_{6r} + id_{6s}$ represent higher-order dispersions [third-order dispersion (TOD), fourth-order dispersion (FOD), fifth-order dispersion (FFOD), and sixth-order dispersion (SOD), respectively]. T_2 is the dipole relaxation time. The relations defining the coefficients are given as follows: $d_{3r} = -4\delta\frac{g_p(1-\delta^2)T_2^3}{2n(1+\delta^2)^4}$, $d_{3s} = -\frac{\beta_3}{6} - \frac{g_p(-1-\delta^4+6\delta^2)T_2^3}{2n(1+\delta^2)^4}$, $d_{4r} = \frac{\beta_4}{24} - \frac{g_p(-5\delta+10\delta^3-\delta^5)T_2^4}{2n(1+\delta^2)^5}$, $d_{4s} = -\frac{g_p(1-10\delta^2+5\delta^4)T_2^4}{2n(1+\delta^2)^5}$, $d_{5r} = -\frac{2g_p\delta(3+3\delta^4-10\delta^2)T_2^4}{2n(1+\delta^2)^6}$, $d_{5s} = \frac{\beta_5}{120} + \frac{g_p(1-15\delta^2+15\delta^4-\delta^6)T_2^5}{2n(1+\delta^2)^6}$, $d_{6r} = -\frac{\beta_6}{720} - \frac{g_p(7\delta-35\delta^3+21\delta^5-\delta^7)T_2^6}{2n(1+\delta^2)^7}$, $d_{6s} = -\frac{g_p(-1+21\delta^2-35\delta^4+7\delta^6)}{2n(1+\delta^2)^7}$. $q_{1r} = \frac{\partial\beta}{\partial|\psi|^2} + (\frac{n_2k_0}{4})A_{\text{eff}}^{-1}$ and $q_{1s} = (\frac{\alpha n_2}{4n})A_{\text{eff}}^{-1}$ represent the Kerr nonlinearity coefficient and the

nonlinear gain (or loss) term, respectively. The parameters $q_{2r} = \frac{1}{2}(\frac{\partial\beta}{\partial|\psi|^4}) + \frac{k_0}{4}(\frac{n_2^2}{2n} + n_4)A_{\text{eff1}}^{-1}$ and $q_{2s} = (\frac{\alpha n_4}{4n})A_{\text{eff1}}^{-1}$ stand for first correction of Kerr effect (saturation when it is negative) and gain absorption, respectively. The parameters $q_{3r} = \frac{1}{6}(\frac{\partial\beta}{\partial|\psi|^6}) + k_0(n_6 + \frac{n_2 n_4}{4n})A_{\text{eff2}}^{-1}$ and $q_{3s} = (\frac{\alpha n_6}{4n})A_{\text{eff2}}^{-1}$ are higher-order correction terms of the nonlinear refractive and nonlinear amplification-absorption gain, respectively. $A_{\text{eff}}^{-1}, A_{\text{eff1}}^{-1}, A_{\text{eff2}}^{-1}, n_4, n_6,$ keep the same definition as in Ref. [30]. It is well known that the inelastic Raman scattering is due to the delayed response of the medium, which forces the pulse to undergo a frequency shift, which is known as self-frequency shift (SFS). The m_{kr} are the intrapulse Raman scattering where $m_{2r} = \frac{1}{2}\frac{\partial\beta}{\partial|\psi|_t^4}$ (quintic) and $m_{3r} = \frac{1}{6}(\frac{\partial\beta}{\partial|\psi|_t^6})$ (septic) are the first- and second-order correction terms of $m_{1r} = \frac{\partial\beta}{\partial|\psi|_t^2}$ (cubic). The effect of self-steepening is due to the intensity-dependent group velocity of the optical pulse, which gives to the pulse a very narrow width in the course of propagation. In our model, the parameters n_{ks} denote self-steepening coefficients, $n_{1s} = \frac{\partial}{\partial_\omega}(\frac{\partial\beta}{\partial|\psi|^2})$ is the cubic term, $n_{2s} = \frac{1}{2}\frac{\partial}{\partial_\omega}(\frac{\partial\beta}{\partial|\psi|^4})$ is the quintic term, and $n_{3s} = \frac{1}{6}\frac{\partial}{\partial_\omega}(\frac{\partial\beta}{\partial|\psi|^6})$ is the septic term.

III. LINEAR STABILITY ANALYSIS

In this section, we investigate the MI, based on Eq. (1). The general idea of linear stability analysis is to perturb the steady-state solution and then analyze whether this small perturbation decays or grows with the propagation. The continuous wave solution (CW) to Eq. (1) is assumed to be of the form

$$U(\xi) = \sqrt{P_0}\exp(i\chi(\xi) - (\gamma_s - i\gamma_r)\xi), \tag{2}$$

where P_0 is the input power of CW, and $\chi(\xi)$ is the nonlinear phase shift given by

$$\begin{aligned}\chi(\xi) = {} & iq_{1r}\left(\int_0^\xi P_0\exp(-2\gamma_s\xi)d\xi\right) \\ & + iq_{2r}\left(\int_0^\xi P_0^2\exp(-4\gamma_s\xi)d\xi\right) \\ & + iq_{3r}\left(\int_0^\xi P_0^3\exp(-6\gamma_s\xi)d\xi\right).\end{aligned} \tag{3}$$

To study the MI phenomena, we add a small perturbation to the CW solution and explore the growth of the perturbation as

$$\begin{aligned}U(\xi,\tau) = {} & (\sqrt{P_0} + u(\xi,\tau) + iv(\xi,\tau)) \\ & \times\exp(i\chi(\xi) - (\gamma_s - i\gamma_r)\xi),\end{aligned} \tag{4}$$

where $u(\xi,\tau)$ and $v(\xi,\tau)$ are the real and imaginary parts of small perturbation, respectively. Substituting Eq. (4) into Eq. (1), and after some mathematical manipulations, we obtain the following set of linearized equations for disturbance behaviors:

$$\begin{aligned}& u_\xi + \sum_{n=2}^{6}(d_{ns}u_{n\tau} + d_{nr}v_{n\tau}) \\ & + P_0(3\,n_{1s} + 5\,n_{2s}P_0A_\xi^2 + 7\,n_{3s}{P_0}^2A_\xi^4)A_\xi^2u_\tau \\ & + 2{P_0}^2\big(q_{2s} + 2\,q_{3s}P_0A_\xi^2\big)A_\xi^4u = 0,\end{aligned} \tag{5}$$

$$\begin{aligned}& v_\xi + \sum_{n=2}^{6}(d_{ns}v_{n\tau} - d_{nr}u_{n\tau}) \\ & + P_0\left[\sum_{n=1}^{3}\big(-2nP_0^{(n-1)}m_{rn}u_\tau + n_{ns}v_\tau\big)A_\xi^{2(n-1)}\right]A_\xi^2 \\ & - 2P_0(q_{1r} + 4\,q_{2r}P_0A_\xi^2 + 6\,q_{3r}{P_0}^2A_\xi^4)A_\xi^2u = 0.\end{aligned} \tag{6}$$

We acknowledge the presence of n_{ns} in those equations and $A_\xi = \exp(\gamma_r\xi)$. To solve the set of linear differential equations above, we assume the following ansatz states [69]:

$$u(\xi,\tau) = u_0\exp\left[i\int K(\xi)d\xi - i\Omega\,\tau\right], \tag{7}$$

$$v(\xi,\tau) = v_0\exp\left[i\int K(\xi)d\xi - i\Omega\,\tau\right], \tag{8}$$

where K and Ω are the wave vectors and the frequency of the perturbation amplitude respectively. Here u_0 and v_0 are the perturbation amplitude of anti-Stokes or backward (if its argument is negative) and Stokes sidebands or forward (if its argument is positive), respectively. Introducing Eqs. (7) and (8) into Eqs. (5) and (6), we obtain a set of two linearly coupled equations satisfied by u_0 and v_0 for nontrivial solutions. The nontrivial solution is such that

$$(K(\xi,\Omega) + g_{rs})^2 = \Gamma + i\Lambda, \tag{9}$$

where the real part of g_{rs} is given as

$$\begin{aligned}g_r = {} & P_0A_\xi^2\big(2n_{1s} + 3A_\xi^2n_{2s}P_0 + 4A_\xi^4n_{3s}{P_0}^2\big)\Omega \\ & + d_{5s}\Omega^5 - d_{3s}\Omega^3,\end{aligned} \tag{10}$$

and the imaginary part is defined as

$$\begin{aligned}g_s = {} & -d_{6s}\Omega^6 + d_{4s}\Omega^4 - d_{2s}\Omega^2 \\ & + {P_0}^2A_\xi^4(2q_{3s}P_0A_\xi^2 + q_{2s}).\end{aligned} \tag{11}$$

Γ and Λ are expressed as the sum of the even and odd orders of Ω, respectively. $\Gamma = \sum_{n=0}^{6}A_{2n}\Omega^{2n}$, and $\Lambda = \sum_{n=1}^{6}A_{2n-1}\Omega^{2n-1}$, A_n coefficients are defined in the Appendix. The roots of Eq. (9) are related to the sign of Λ. We will obtain two distinguishable cases:

(i) $\Lambda < 0$, the expressions of these roots are written as

$$K_1(\xi,\Omega) = g_r + h_1 + i(g_s - h_2), \tag{12}$$

$$K_2(\xi,\Omega) = g_r - h_1 + i(g_s + h_2), \tag{13}$$

where

$$h_1 = \sqrt{\tfrac{1}{2}(\Gamma + \sqrt{\Gamma^2 + \Lambda^2})},$$

$$h_2 = \sqrt{\tfrac{1}{2}(-\Gamma + \sqrt{\Gamma^2 + \Lambda^2})}.$$

(ii) $\Lambda > 0$, we have

$$K_1^*(\xi,\Omega) = g_r - h_1 + i(g_s - h_2), \tag{14}$$

$$K_2^*(\xi,\Omega) = g_r + h_1 + i(g_s + h_2), \tag{15}$$

leading to solutions with the same asymptotic behavior as those obtained from K_1 and K_2. The complex forms of K_1

and K_2 make it difficult to predict their signs. Nevertheless, their imaginary parts contribute to the system. Introducing Eq. (14) into two ansatzes, Eqs. (7) and (8) provide a good and clear understanding of the behavior of these wave solitons. The quantity h_2 is always positive, that is, $g_s - h_2 < g_s + h_2$ holds, and this behavior depends on the sign of the quantity $g_s - h_2$ which corresponds to the imaginary part of K_1. The asymptotic behavior of Eqs. (7) and (8) is related to the constant $g_s - h_2$. If $g_s < 0$, then $h_2 - g_s$ is always positive and the solution of Eqs. (7) and (8) increases exponentially when ξ goes toward to infinity. The system remains unstable under modulation. In this case, the boundaries of the domain of the MI are then given by $-\Omega_0(\xi) \ll \Omega(\xi) \ll \Omega_0(\xi)$, where

$$\Omega_0^2(\xi) = \sqrt[3]{C_0 + \frac{C_1}{18}} + \sqrt[3]{C_0 - \frac{C_1}{18}} + \frac{d_{6s}}{3d_{4s}}. \tag{16}$$

If $g_s > 0$, the asymptotic behavior of wave solution will depend on the sign of $h_2 - g_s$.

When $\omega = \omega_0$, it is easy to distinguish two cases. For $h_2 - g_s > 0$, i.e., $g_s - h_2 < 0$ and $I_m(K_1) < 0$, where $I_m(K_1)$ represents the imaginary part of K_1, the solutions Eqs. (7) and (8) diverge without limitation as ξ increases and the corresponding solution is said to be modulationally unstable. The criterion for the modulation instability of Stokes waves is such that

$$0 > -\frac{\left(2g_s^2 - h_{11}\right)}{2P\Omega^2} > -Y + d_{2r}q_{1r} - d_{2s}q_{1s}, \tag{17}$$

where h_{11} is defined as

$$h_{11} = -18\,P_0^6 {q_{3s}}^2 - 24\,P_0^5 q_{2s}q_{3s} + \left(-8\,{q_{2s}}^2 - 12\,q_{3s}q_{1s}\right)P_0^4 - 8\,P_0^3 q_{2s}q_{1s} - 2\,P_0^2 {q_{1s}}^2,$$

where $Y = Y_{11} + Y_0 + 2(d_{4s}q_{2s} - d_{4r}q_{2r})P_0\Omega^2 + 3(d_{6r}q_{3r} - d_{6s}q_{3s})P_0^2\Omega^4$, with

$$Y_0 = {d_{6r}}^2\Omega^{12} + {d_{4r}}^2\Omega^8 + {d_{5s}}^2\Omega^{10} + {d_{3s}}^2\Omega^6 + {d_{2r}}^2\Omega^4 + \left(25\,{n_{s3}}^2P_0^6 + 13\,{n_{s2}}^2P_0^4\right)\Omega^2,$$

and Y_{11} is given in the Appendix. From Lange-Newell's criterion, our system is such that

$$-Y_{11} + d_{2r}q_{1r} - d_{2s}q_{1s} + 2(d_{4s}q_{2s} - d_{4r}q_{2r})P_0\Omega^2 + 3(d_{6r}q_{3r} - d_{6s}q_{3s})P_0^2\Omega^4 < 0. \tag{18}$$

It is important to recall that Lange-Newell's criterion was derived for the first time for the Hamiltonian system in Ref. [70], and for discrete and continuous dissipative systems [71–73]. The numerical results from the previous analytical treatments are presented below.

IV. NUMERICAL SIMULATIONS

Theoretical investigation of MI through the model under consideration indicates the possibility of observing instability regions in the frequency spectra. The MI spectra are given by the negative imaginary part of the dispersion relation. In this study, we have two possibilities to obtain the MI gain. First, when $\omega_0 = \omega_a$, the growth rate is defined as

$$g(\Omega) = 2(g_s + h_2), \tag{19}$$

and when $\omega_0 \neq \omega_a$, the growth rate is given in the following integral form [16,69]

$$g(\Omega) = -2\int_0^L (g_s + h_2)d\xi, \tag{20}$$

which is referred to as the integrated MI. Although this analysis is necessary, it is however limited since it does not describe the long-time evolution of the MI phenomenon. This requires results from the linear stability analysis to be confronted with direct numerical simulations. This is done on Eq. (1) via the split-step Fourier method with the initial condition being taken as [69]

$$\psi(0,\tau) = \sqrt{P_0}[1 + a_m \sin(f_m\tau)]\exp(i\phi_{NL}), \tag{21}$$

with

$$\phi_{NL} = \frac{P_0}{2\gamma_s}\left(q_{1r} + \frac{q_{2r}P_0}{2} + \frac{q_{3r}{P_0}^2}{3}\right),$$

where P_0 is the power, a_m and f_m are, respectively, the modulation amplitude and frequency of a weak sinusoidal perturbation imposed on the CW beam. We use sensitivity analysis (SA) to observe simultaneous physical effects on the boundary conditions of the domain of the MI [74–77].

A. Cubic-quintic-septic complex Ginzburg-Landau (CQSCGL) equation

Here, all dispersion coefficients beyond the second order are set to zero, i.e., $d_{jrs} = m_{kr} = n_{ks} = 0$ for $j > 2$ and $k > 1$. This reduces Eq. (1) to the cubic-quintic-septic CGL equation. This physical situation corresponds to the cubic-quintic CGL equation, with the septic nonlinearity being a correction term. It appears in physical processes of strong focusing nonlinearity. It is also essential to study the impact of q_{3r} and q_{3s} terms on MI. From the Lange-Newell criterion, the boundary of the domains of the MI is such that $\Omega^2 < \Omega_c^2$, where Ω_c^2 is the critical frequency of the disturbing wave defined as

$$\Omega_c^2 = 2d_{2s}^{-2}(q_{1s}d_{2s} - q_{1r}d_{2r})P_0 + 4d_{2s}^{-2}(q_{2s}d_{2s} - q_{2r}d_{2r})P_0^2 + 6d_{2s}^{-2}(q_{3s}d_{2s} - q_{3r}d_{2r})P_0^3, \tag{22}$$

corresponding to $\omega_0 = \omega_a$. In this paper, we will focus only on the normal regime, i.e., $d_{2r} < 0$, associated with the following values of parameters: $q_{1r} = 5 \times 10^{-1}$, $q_{1s} = -48 \times 10^{-2}$, $q_{2r} = -34 \times 10^{-2}$, $q_{2s} = -34 \times 10^{-2}$, $d_{2r} = -0.5$, $d_{2s} = 0.1$, $\gamma_s = -3 \times 10^{-3}$, $L = 1500$, $f_m = 95 \times 10^{-2}$ and $a_m = 95 \times 10^{-3}$. Although some values of parameters have been taken arbitrarily, they remain, nevertheless, closer to experimental values available in the literature [8,30,35,65,69]. Figure 1 shows the MI spectrum as a function of second-order correction of Kerr nonlinearity and nonlinearity gain and loss, respectively. More precisely, Figs. 1(a) and 1(b) show the MI gain as a monotonously increasing function septic non-Kerr nonlinearity. We observe uniform shapes of gain with an increase of septic gain-loss coefficient. In addition, two regions of instability of MI gain in the two diagrams above will appear. We also note that q_{3s} increases the MI more than q_{3r}. This result is confirmed in Fig. 2, which illustrates the simultaneous physical effect on the boundary domain of MI. This result is obtained by sensitive analysis, where sampled physical parameter values appear

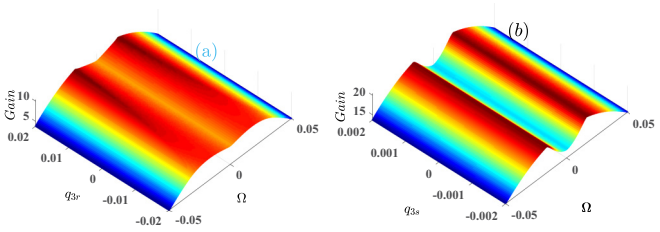

FIG. 1. Instability gain spectra [Gain(m^{-1}), Ω(THz)] of CQSCGLE for $P_0 = 1$, $\gamma_r = -9 \times 10^{-3}$: (a) $q_{3s} = 1$, (b) $q_{3r} = 5 \times 10^{-1}$.

in Eq. (22). With this method, we have been able to obtain well-known results such as the growth of MI with an increase of the power input P_0 and the Kerr nonlinearity q_{1r}. At the same time, the first-order correction of gain nonlinearity q_{2s} reduces the critical frequency, consequently reducing MI. We also observe a moderate influence of spectral filtering d_{2s}, dispersion d_{2r}, gain-loss q_{1s}, and quintic coefficient q_{2r}. To understand the physical effects of q_{3r} and q_{3s}, we introduce Eq. (21) into Eq. (1) and observe the numerical evolution of the perturbed plane wave. Figure 3 illustrates the propagation of CW in the CQSCGLE. Figure 3(a) shows the profile of CW in the plane (ξ, τ), while in Fig. 3(b), we plotted the transverse distribution of the wave's intensity $\xi = 1m$ (dashed line), $\xi = 225m$ (dotted line), and $\xi = 1200m$ (solid line). Initially, the plane wave has periodic transverse evolution near the origin. Then, at $\xi = 225m$, the intensity decreases, and subpulses emerge between two pulses. So far, the intensity of CW increases, and we observe a few generations of subpulses. The CW presents a chaotic behavior along with the distance of propagation. This is considered as a numerical property of MI in a dispersive medium that could not be predicted by the linear stability analysis [16]. Figure 3(c) shows the evolution of CW when $q_{3r} < 0$ (defocusing case), and Fig. 3(d) depicts the evolution of energy (solid line) and center of mass (dashed line). These two quantities were already used in the bifurcation study of creeping solitons in dissipative systems [6].

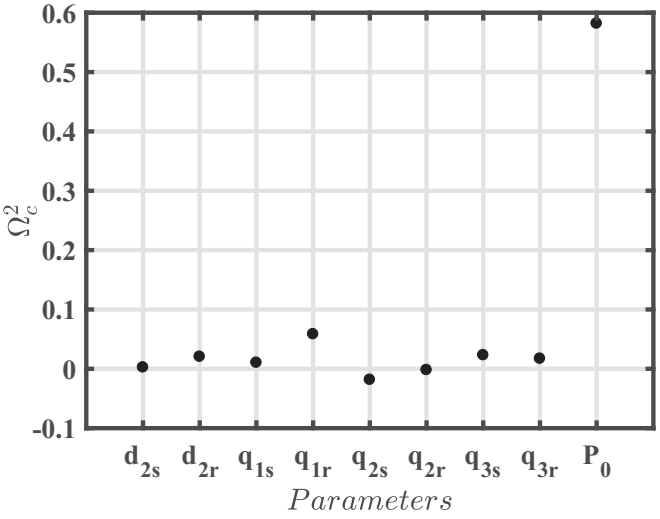

FIG. 2. Influence of some physical effects on the frequency of the disturb wave using the sensitive analysis.

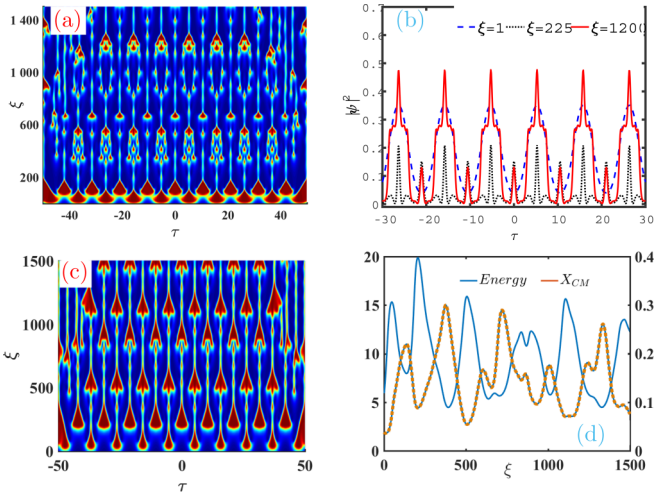

FIG. 3. Second-order correction effect of Kerr nonlinearity on continuous wave propagation [$\xi(m), \tau(ps)$]. Focusing case: (a) Propagation of CW. (b) Distribution of intensity for $q_{3r} = 3 \times 10^{-1}$. Defocusing case: (c) Propagation of CW. (d) Comparison of energy and center of mass for $q_{3r} = -3 \times 10^{-1}$.

Here, the position corresponding to the maxima of energy and dips of center of mass are the positions where the MI induces the solitons. Note that the energy and center of mass are defined as

$$Q = \int_{-\infty}^{\infty} |\psi(\xi, \tau)|^2 d\tau,$$
$$X_{\text{c.m.}} = \frac{\int_{-\infty}^{\infty} \tau |\psi(\xi, \tau)|^2 d\tau}{Q}. \tag{23}$$

The second order of correction of Kerr nonlinearity presents excellent advantages in dissipative systems.

B. Effects of higher-order dispersion coefficients

In this section, attention is paid to the effects of higher-order complex dispersion coefficients on MI. Such physical situations take place in optical fibers with zero-dispersion wavelength.

1. Effect of the complex fourth-order dispersion coefficient

We consider the optical fiber with complex third-order dispersion (TOD) and fourth-order dispersion (FOD) with the septic nonlinearity. The propagation model is equivalent to the modified complex Swift-Hohemberg equation (mCSHE), where $(d_{3r} + id_{3s})$ will be considered the lower-order correction of linear terms, γ_r is the real linear loss, while the septic term conserves its value used previously.

Figure 4 illustrates the MI gain spectrum as a function of correction term d_{3r}. It appears that the integrated gain conserves its two lobes of instability. As depicted in Fig. 4(a), we observe an increase of d_{3r}, which causes the gain to increase up to a maximum value, and thereafter decreases. We note that this maximum value is obtained near the zero correction term. For a better explanation of that phenomenon, Fig. 4(b) shows the variation of the integrated gain as a function of the perturbation frequency Ω for different values of d_{3r}. The

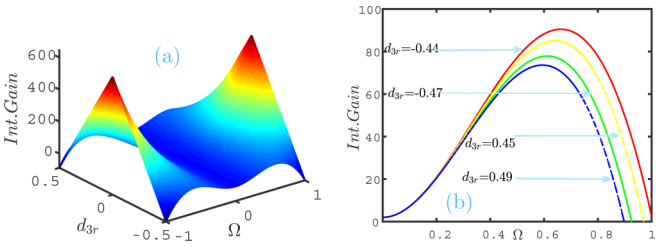

FIG. 4. (a) 3D surface plot showing the integrated gain in the plane (Ω, d_{3r}). (b) Integrated gain in the plane (0, Ω) for the various values of d_{3r}, for $P_0 = 5 \times 10^{-3}$, $d_{3s} = 4 \times 10^{-2}$, $d_{4r} = 0$, $d_{4s} = -8 \times 10^{-3}$. The other parameters are the same as in Fig. 1.

integrated gain increases and decreases with the increase of the lower order correction terms. Figure 5 shows the evolution of MI beneath the correction effects. The subsequent evolution of the pulse train along the propagation distance is displayed in Fig. 5(a). In Fig. 5(b), the energy for two different values of the correction term is computed, and the dashed curve is obtained for $d_{3r} = -15 \times 10^{-3}$. Interestingly, the magnitude of the energy decreases as the wave train propagates, while the magnitude of energy increases with ξ, and the number of maxima gets higher. It is also of importance to quantify the number of solitons induced by MI for two different values of the physical effect. This is done using the bifurcation diagram.

Figure 6 depicts the maxima (referred to as $Q_{\max}$) and minima (referred to as $Q_{\min}$) of energy as a function of d_{3r}. The positions of the generation of solitons induced by the MI are indicated as the maxima of $Q_{\max}$. It is also clear from the diagram that the mCSHE produces many solitons with high energy for some values of the correction terms. Depending on the value of d_{3r}, we observe that one, two, three, and four solitons having different energy can be generated simultaneously within the same propagation distance.

That means that the lower-order correction term must not be neglected in optical fiber communications.

Along the same line, Fig. 7 depicts the integrated MI gain against the frequency Ω and the fourth-order dispersion coefficient d_{4r}. The integrated MI gain is the same for positive and negative values of the frequency Ω for some selected values of the fourth-order dispersion (FOD) d_{4r}, as shown in Fig. 7(b). Figure 8 shows the evolution of the CW (inducing the MI [see

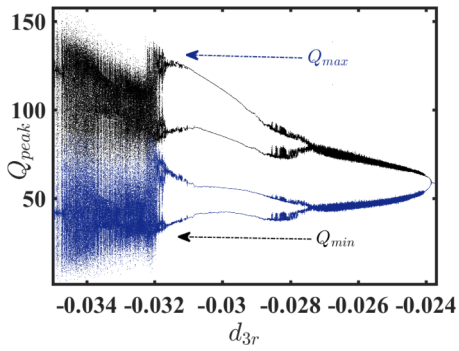

FIG. 6. Bifurcation diagram as a function of the dopant effect. The physical parameters are the same as in Fig. 5.

Fig. 8(a)] and the energy as a function of the higher-order spectral filtering d_{4s} [see Fig. 8(b)]. It appears that the MI is the precursor of the propagation of solitons in mCSHE.

2. *Effects of higher-order dispersion correction*

Taking into account higher-order dispersion terms brings additional terms to the CSH equation. We note strong dependence of dopant effect through d_{5r}, which requires more attention to be paid to the fifth-order dispersion. Like the third-order d_{3r}, the fifth-order d_{5r} produces similar behaviors on the MI gain spectrum as confirmed by Fig. 9, which shows the MI spectrum as a function of the high linear dopant effect. In Fig. 9(a), an increase and a decrease of the integrated gain, with increasing values of the d_{5r}, is noticed. Figure 9(b) shows the maximum gain against the fifth-order dispersion. The pyramidal form of the maximum gain is obtained near the zero value of d_{5r}. The outcome of the MI excitation is confirmed by the generation of train of pulses in the medium [see Fig. 10(a)], along with the bifurcation diagram as a function of parameter d_{5r} [see Fig. 10(b)].

3. *Sixth-order dispersion effect*

We now consider the sixth-order complex dispersion term $(d_{6r} + id_{6s})$. The integrated MI gain maintains its shape by increasing the value of d_{6r}. The results are displayed in Fig. 11. The peak of integrated gain near zero is shown in Fig. 11(b), while the bandwidth decreases when the value of

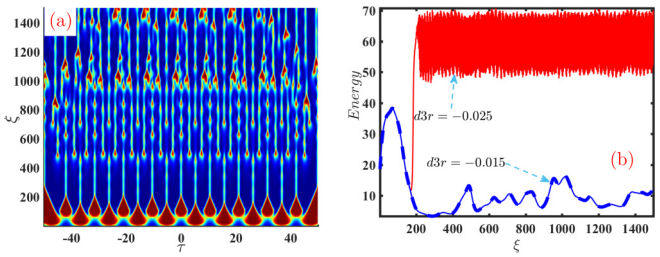

FIG. 5. (a) Propagation of the perturbed wave. (b) Effect of dopant through the energy $d_{3r} = -25 \times 10^{-3}$ (solid line), $d_{3r} = -15 \times 10^{-3}$ (dashed line); the other physical parameters are $[\xi(m), \tau(ps)]$: $P_0 = 1$, $q_{3r} = 3 \times 10^{-1}$, $q_{3s} = 1$, $d_{3s} = 0.04$, $d_{4r} = 0$, $d_{4s} = -8 \times 10^{-3}$, $\gamma_r = -99 \times 10^{-4}$.

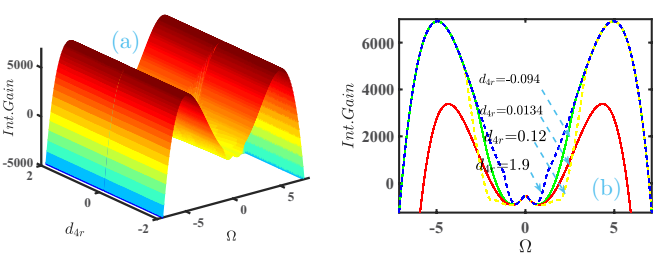

FIG. 7. (a) 3D surface plot showing the integrated gain in the plane (Ω, d_{4r}). (b) Integrated gain as a function of the frequency Ω for various values of fourth-order dispersion coefficients for $P_0 = 5 \times 10^{-2}$, $q_{3r} = 5 \times 10^{-1}$, $q_{3s} = 1$, $d_{3s} = -1 \times 10^{-2}$, $d_{3r} = -1 \times 10^{-2}$, $d_{4s} = 2 \times 10^{-3}$, $\gamma_r = -9 \times 10^{-3}$.

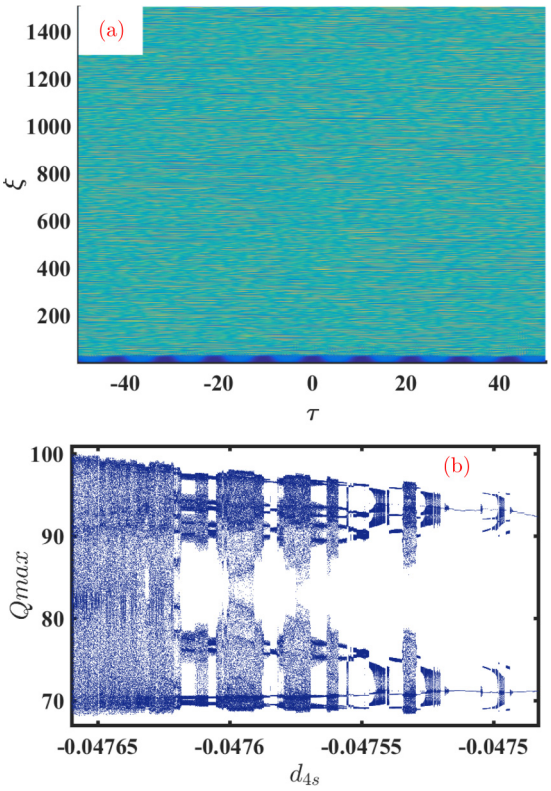

FIG. 8. (a) Evolution $[\xi(m), \tau(ps)]$ of the modulational instability when (a) $d_{4s} = -6 \times 10^{-2}$, and $P_0 = 1$, $q_{3r} = 3 \times 10^{-1}$, $q_{3s} = 1$, $d_{3r} = d_{3s} = -1 \times 10^{-2}$, $\gamma_r = -99 \times 10^{-4}$. (b) Map soliton induced as a function of higher-order spectral filtering.

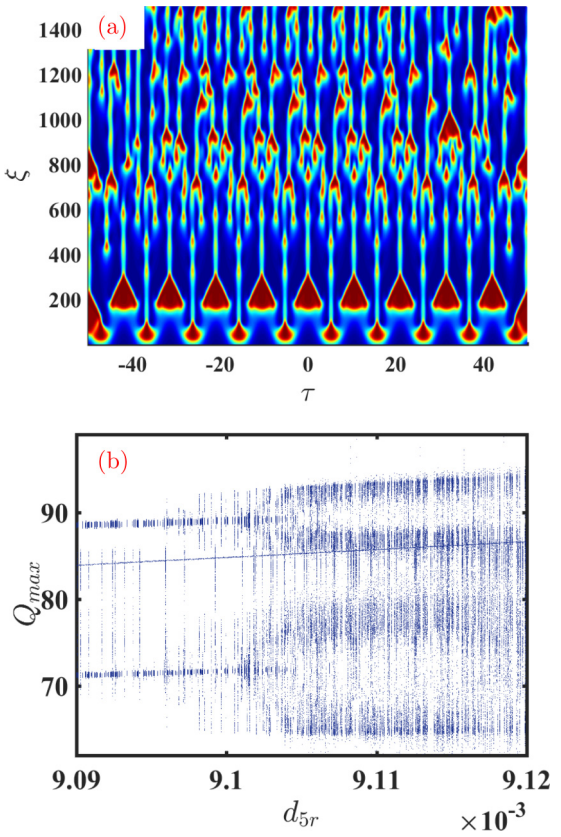

FIG. 10. (a) Evolution $[\xi(m), \tau(ps)]$ of modulation instability for $d_{5r} = 7 \times 10^{-3}$, and $P_0 = 1$, $q_{3r} = 8 \times 10^{-1}$, $q_{3s} = 1.5$, $d_{3r} = d_{3s} = -1 \times 10^{-1}$, $d_{4r} = -2 \times 10^{-2}$, $d_{4s} = -2 \times 10^{-2}$, $d_{5s} = -1 \times 10^{-3}$, $\gamma_r = -99 \times 10^{-4}$. (b) Map soliton induced as a function of higher-order dopant effect d_{5r}.

d_{6r} increases. The solid line illustrates the growth rate near zero.

Due to the large space of parameter values, Fig. 12 shows an example of the stability investigation of the continuous wave in the (d_{6r}, q_{3r}) plane [see Fig. 12(a)]. The white area indicates the domain of stability, and the blue regions correspond to unstable zones. When we consider a point in the zone of stability, the CW keeps its stability ($\xi = 1170m$) and oscillates periodically as it can be seen from Fig. 12(b). When taking a point in the instability area, the CW disintegrates, as shown by the dashed line in Fig. 12(b), which is indeed a signature of its instability. In Fig. 13, we plot the intensity distribution as a function of the retarded time τ, at the propagation distance $\xi = 1200m$. Only the case with even dispersion (see solid line in Fig. 13) and the full dispersion (see dashed line in Fig. 13) are illustrated. As a whole, higher values of the intensity distribution are obtained when considering the even dispersions coefficients. We also note the presence of subpulses. In this case, the amplitude of CW is high, and the transverse distribution is symmetric. In Fig. 14,

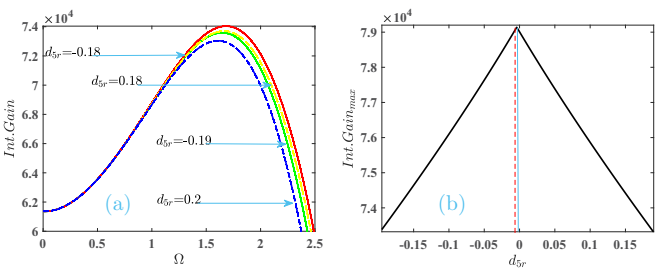

FIG. 9. Effect of higher-order dopant on the instability spectrum. (a) Integrated gain as a function of Ω. (b) Maximum integrated gain as a function of d_{5r}, with $\Omega_{\max}(\mathrm{THz}) = 1.6$. The parameters used are $P_0 = 5 \times 10^{-1}$, $q_{3r} = 5 \times 10^{-1}$, $d_{3r} = d_{3s} = -1 \times 10^{-2}$, $d_{4r} = -5 \times 10^{-2}$, $d_{4s} = -2 \times 10^{-2}$, $d_{5s} = -1 \times 10^{-3}$, $\gamma_r = -9 \times 10^{-3}$.

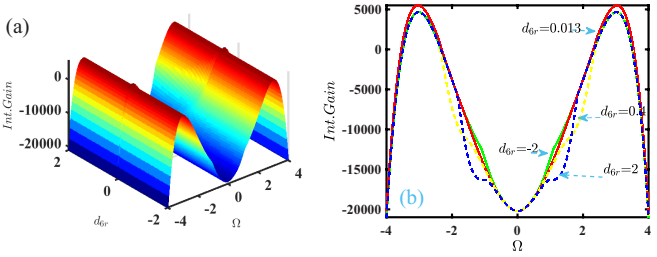

FIG. 11. (a) 3D surface plot showing the integrated gain, in the plane (Ω, d_{6r}); (b) integrated gain as a function of the frequency Ω, for the various of sixth-order of dispersion coefficient for $P_0 = 2 \times 10^{-1}$, $q_{3r} = 5 \times 10^{-1}$, $q_{3s} = 5 \times 10^{-1}$, $d_{2r} = -5 \times 10^{-1}$, $d_{2s} = 5 \times 10^{-1}$, $d_{3r} = d_{3s} = -1 \times 10^{-2}$, $d_{4r} = -1 \times 10^{-2}$, $d_{4s} = -18 \times 10^{-3}$, $d_{5r} = -9 \times 10^{-3}$, $d_{5s} = -1 \times 10^{-3}$, $d_{6s} = 55 \times 10^{-4}$, $\gamma_r = -9 \times 10^{-4}$.

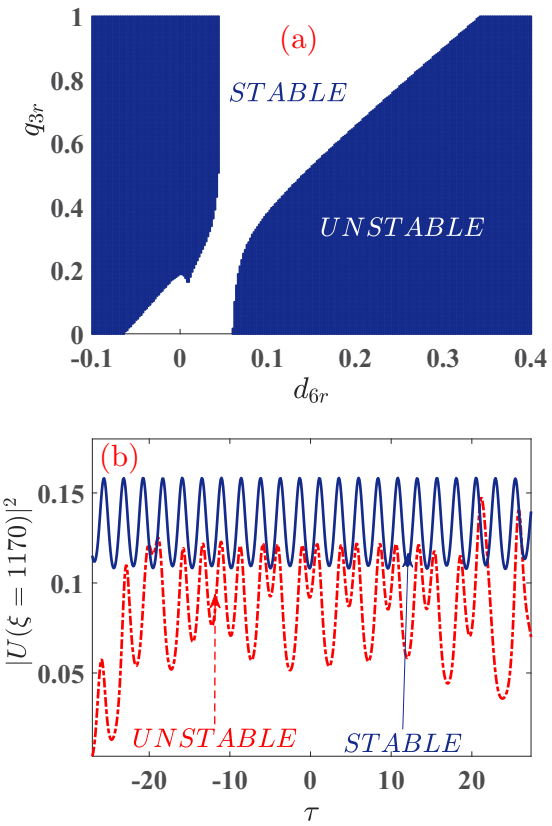

FIG. 12. (a) The chart of stability. (b) Transversal distribution of the modulation instability at $\xi = 117 \times 10^1 m$ for modulation stable (solid line) and modulation unstable (dashed line). The physical parameters are $P_0 = 2 \times 10^{-1}$, $q_{3s} = 4 \times 10^{-1}$, $d_{3s} = d_{3r} = -1 \times 10^{-2}$, $d_{4r} = -2 \times 10^{-2}$, $d_{4s} = -18 \times 10^{-3}$, $d_{5r} = 9 \times 10^{-3}$, $d_{5s} = -4 \times 10^{-3}$, $d_{6s} = -9 \times 10^{-4}$, $\gamma_r = -99 \times 10^{-4}$, and (b) solid line ($d_{6r} = 0$; $q_{3r} = 0$), dashed line ($d_{6r} = 4 \times 10^{-1}$, $q_{3r} = 1$).

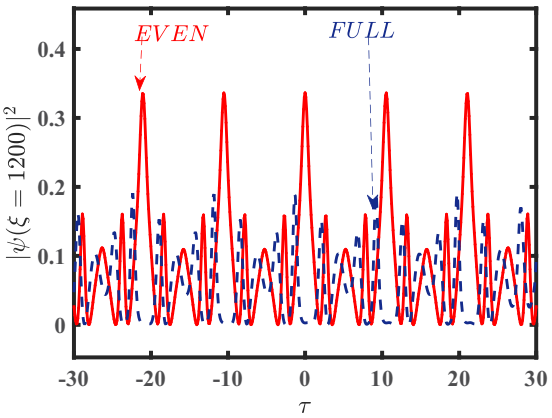

FIG. 13. Transversal distribution of the modulation instability at $\xi = 12 \times 10^2 m$ for even dispersion (solid line) and full dispersion (dashed line). The physical parameters are $P_0 = 1$, $q_{3s} = 1$, $q_{3r} = 4 \times 10^{-3}$, $d_{3s} = d_{3r} = -1 \times 10^{-2}$, $d_{4r} = -2 \times 10^{-2}$, $d_{4s} = -2 \times 10^{-2}$, $d_{5r} = 89 \times 10^{-4}$, $d_{5s} = -1 \times 10^{-3}$, $d_{6s} = -9 \times 10^{-4}$, $d_{6r} = -1 \times 10^{-4}$, $\gamma_r = -99 \times 10^{-4}$.

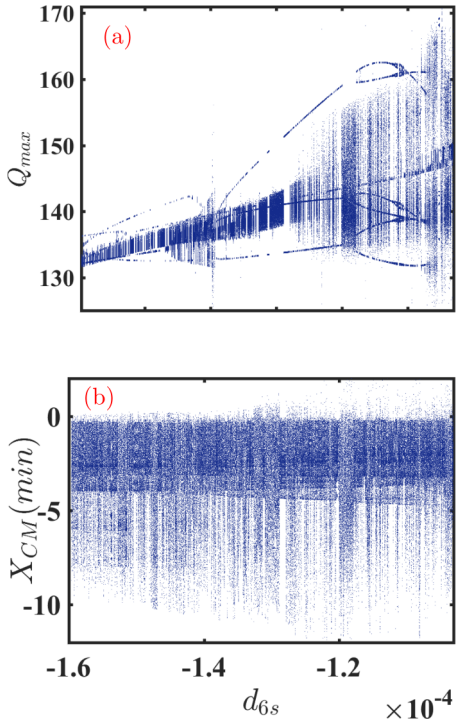

FIG. 14. Comparison of map solitons as a function of higher-order d_{6s} term through (a) energy and (b) center of mass.

we compare the map of solitons as a function of d_{6s} effect through energy [see Fig. 3(d)] and the dips of center of mass [see Fig. 14(b)]. These results are in good agreement with those from Fig. 3(d).

C. Effect of intrapulse Raman scattering and their correction terms

Here, we further analyze the influence of self-frequency shift and their correction terms on the MI using the CQSCGL equation with higher-order dispersions. The self-frequency shift effect is generally presented as the gradient of nonlinearity, which brings about additional instability regimes on MI [78]. Figure 15 shows the integrated MI gain as a function of the input power P_0, taking into account the self-

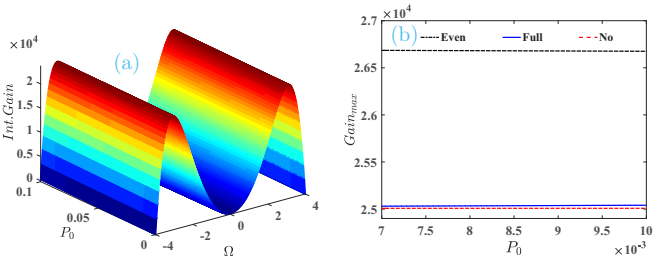

FIG. 15. (a) 3D surface plot showing the integrated gain, in the plane (Ω, P_0). (b) Maximum gain as a function of P_0, with $\Omega_{\max}(\mathrm{THz}) = 3.1$, for different physical situations. The parameters are $q_{3r} = 4 \times 10^{-1}$, $q_{3s} = 1$, $d_{3r} = d_{3s} = -1 \times 10^{-2}$, $d_{4r} = -1 \times 10^{-2}$, $d_{4s} = -2 \times 10^{-2}$, $d_{5r} = 6 \times 10^{-3}$, $d_{5s} = -1 \times 10^{-3}$, $d_{6s} = -6 \times 10^{-2}$, $d_{6r} = 6 \times 10^{-3}$, $\gamma_r = -1 \times 10^{-3}$, $m_{1r} = 6 \times 10^{-1}$, $m_{2r} = 8 \times 10^{-2}$, $m_{3r} = 5 \times 10^{-3}$.

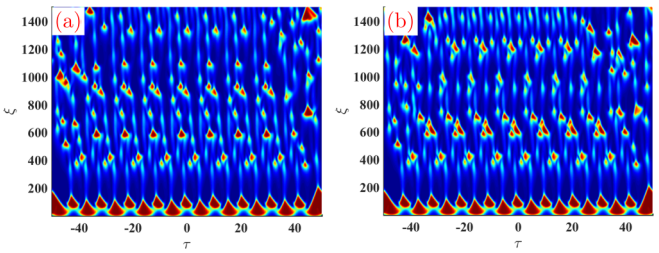

FIG. 16. Evolution $[\xi(m), \tau(ps)]$ of modulational instability in the presence of self-frequency shift effect and their two correction terms. (a) Full dispersion. (b) Even dispersions. The other parameters are: $P_0 = 1,\ m_{1r} = 6 \times 10^{-1},\ m_{2r} = 8 \times 10^{-2},\ m_{3r} = 5 \times 10^{-3}$.

frequency shift effect associated with even dispersion effects (dark dashed line), the full dispersion effects (solid blue line). Neglecting the self-frequency shift contribution, the result is displayed by the red dotted lines. The numerical evolution of the CW inducing the MI in this regime is illustrated in Fig. 15. Figure 16(a) shows the case of full dispersion coefficient, and Fig. 16(b) gives results when the dispersion coefficients are even. For the second case, we observe a pronounced concentration of train of pulses at $\xi = 6 \times 10^2 m$.

From the above, it is evident that the self-frequency shift and their correction terms increase the gain of instability, and this is higher when including the even complex dispersions.

D. Effect of higher-order term of self-steepening

Here, we study in detail the effect of self-steepening with correction terms on the MI using the CQSCGLE with higher-order complex dispersion coefficients. Neglecting the impact of the self-frequency and their correction terms, Fig. 17 shows the maximum gain as a function of the input power P_0, where solid line represents the maximum gain with full complex dispersion coefficients and dotted lines represent the case when even dispersion is considered.

Figure 18 illustrates the propagation of the CW in the presence of self-steepening in two dispersion cases. In Fig. 18(a), we investigated the case of full dispersion, where it appears

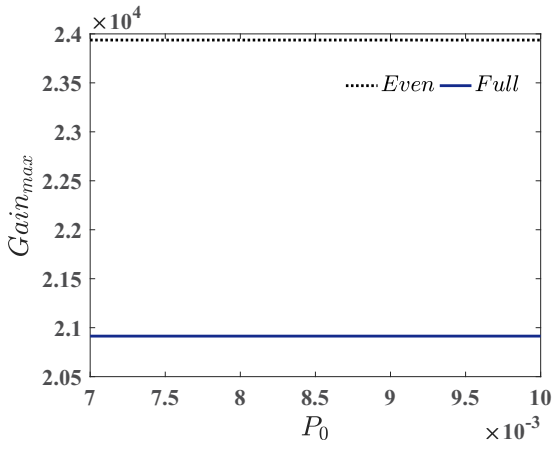

FIG. 17. The maximum gain as a function of power P_0 with $\Omega_{\max}(\mathrm{THz}) = 3.1$, for different physical situations. The physical parameters are $n_{1s} = 4 \times 10^{-1},\ n_{2s} = 8 \times 10^{-2},\ n_{3s} = 8 \times 10^{-3}$.

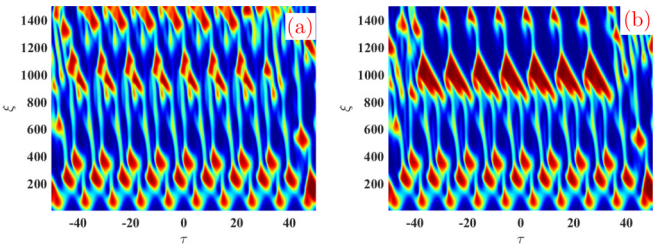

FIG. 18. (a) Evolution $[\xi(m), \tau(ps)]$ of modulational instabilty in the presence of self-steepening effect and their two correction terms. (a) Full dispersion. (b) Even dispersions. The other parameters are $P_0 = 1,\ n_{1s} = 2 \times 10^{-1},\ n_{2s} = 1 \times 10^{-2},\ n_{3s} = 1 \times 10^{-3}$.

that more trains of optical pulses are generated from the early stage of MI propagation.

The map of the soliton obtained through the center of mass versus the self-steepening n_{1s} is shown in Fig. 19. Based on the corresponding bifurcation diagram, several solitons are induced for different values of n_{1s}.

E. Full model

In this section, the emergence of wave patterns under the activation of MI is studied in the full model equation (1). Note that the critical frequency boundary of the MI has been determined analytically in Eq. (21), which does not depend on the real parts of dispersion and nonlinearity gradient coefficients. Figure 20 presents the statistical diagram showing the degree of influence of the different physical parameters that come into consideration on the boundaries of the frequency domain of the MI. Note that taking the horizontal line corresponding to the critical perturbation frequency at zero, the boundary domains of the MI decrease due to physical effects related to the presence of some points under this horizontal line, whereas the points above the line increase the MI frequency domain.

We also note that the higher-order of spectral filtering increases the boundaries of the MI more than any other physical effect. The boundary domain of the MI is more sensitive to d_{4s}, d_{6s} and the propagation distance ξ. To investigate the MI, we show in Fig. 21(a) the dependence of the MI gain

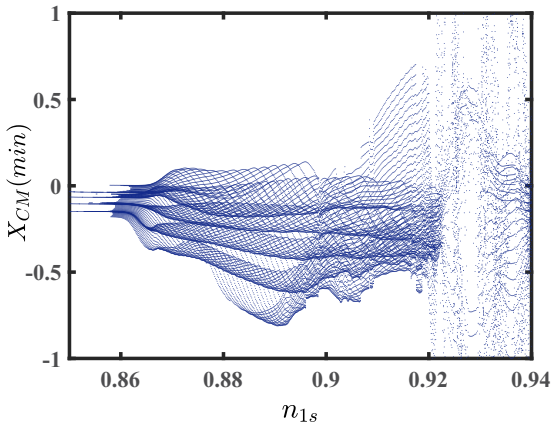

FIG. 19. Map soliton through the dips of the center-of-mass as a function of the self-steepening n_{1s}.

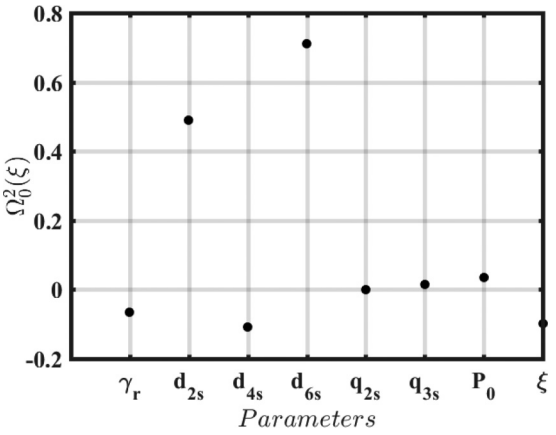

FIG. 20. Influence of the physical parameters on the critical frequency using sensitive analyses.

against P_0 and temporal detuning frequency Ω. In Fig. 21(b), we observe the influence of the input power in the MI gain spectrum. For small values of the input power, the instability gain does not exist at Ω. An increase of the input power leads to an increase of the instability gain associated with two symmetrical side lobes that maintain their shapes. In Fig. 21(c), we observe the profile of the integrated MI gain as a function of Ω, and d_{4r}. In Fig. 21(d), we have three regions of instability (the first is located around the zero frequency $\Omega(\mathrm{THz}) = 0$, and the two others are symmetric from the zero frequency) for a value of $d_{4r} = -3$. The region of instability associated with

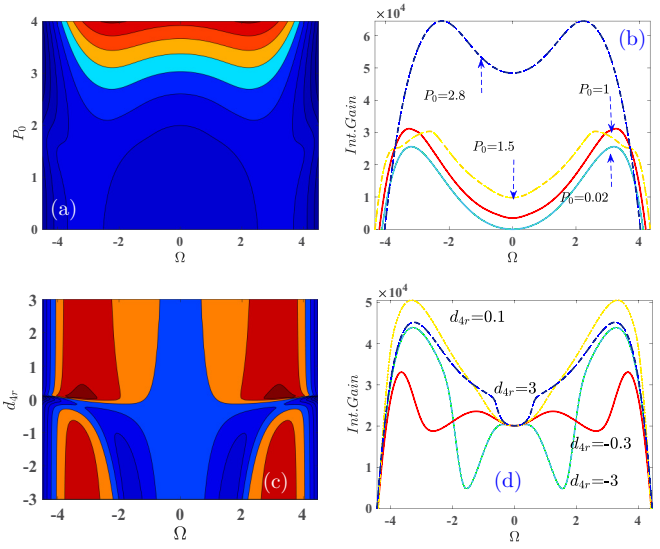

FIG. 21. (a) 2D surface plot showing the integrated gain, in the plane (Ω, P_0.) (b) 2D plot for various values of P_0. when $d_{4r} = -2 \times 10^{-2}$. (c) 3D surface plot showing the integrated gain, in the plane (Ω, d_{4r}), when $P_0 = 1$. (d) 2D a plot as a function of Ω for various values of d_{4r}. Parameters are $q_{3s} = 1$, $q_{3r} = 4 \times 10^{-1}$, $d_{3r} = -34 \times 10^{-3}$, $d_{3s} = -1 \times 10^{-2}$, $d_{4s} = -48 \times 10^{-3}$, $d_{5r} = 8 \times 10^{-3}$, $d_{5s} = -1 \times 10^{-3}$, $d_{6s} = -3 \times 10^{-3}$, $d_{6r} = 6 \times 10^{-3}$, $\gamma_r = -99 \times 10^{-4}$, $n_{1s} = 2 \times 10^{-1}$, $n_{2s} = 5 \times 10^{-3}$, $n_{3s} = 2 \times 10^{-3}$, $m_{1r} = 6 \times 10^{-1}$, $m_{2r} = 8 \times 10^{-2}$, $m_{3r} = 1 \times 10^{-3}$.

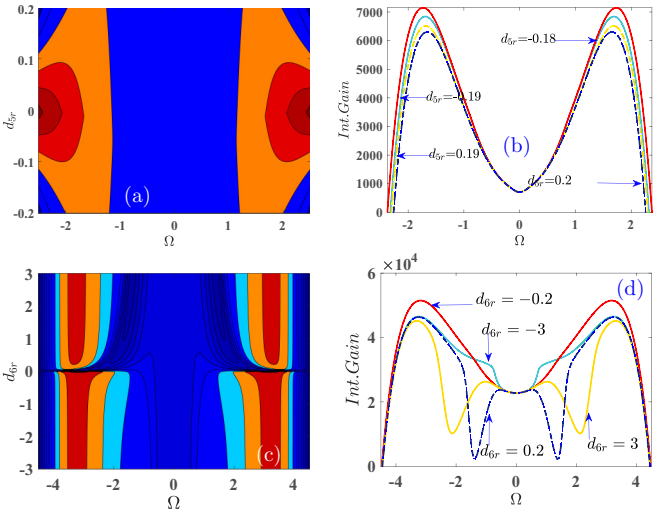

FIG. 22. (a) 2D surface plot showing the integrated gain, in the plane (Ω, d_{5r}) when $d_{6r} = 6 \times 10^{-3}$. (b) 2D plot for the various value of d_{5r}. (c) 2D surface plot showing the integrated gain, in the plane (Ω, d_{6r}), when $d_{5r} = 8 \times 10^{-3}$. (d) 2D plot as a function of Ω for various values d_{6r} Parameters are as follows: $P_0 = 5 \times 10^{-1}$, $d_{4r} = -2 \times 10^{-2}$, and the other parameters are the same as in Fig. 21.

the gain is highly affected by the values of d_{4r} as it is obvious in Fig. 22(d) for $d_{4r} = -3 \times 10^{-1}$ and $d_{4r} = 1 \times 10^{-1}$.

Figure 22 shows the plot of the integrated MI gain as a function of the higher-order dispersion coefficients d_{5r} and the frequency of the perturbation amplitude Ω. In Figs. 22(a) and 22(b), an instability gain is developed, induced by two higher-order dispersion coefficients, d_{5r}.

Figure 22(c) depicts the variation of the instability region. As we can see, reversed phenomena from Fig. 22(d) are observed. Results from numerical simulations of the full model equation of the CW are shown in Fig. 23. Figure 23(b) gives the profile of CW for $P_0 = 1$. Also shown is the distribution of instability at $\xi = 1222m$.

V. CONCLUSION

We have exclusively reported the relationship between the theory of MI and the bifurcation theory of solitons in doped optical fibers through indicators like the bifurcation diagram and the energy. From a cubic-quintic-septic complex Ginzburg-Landau equation with higher-order dispersion and gradient terms, the linear stability analysis has been used to find the expression of the MI gain, along with boundary domains of MI. Moreover, an extended Lange-Newell criterion for the stability and/or instability of Stokes waves has been obtained. In a comprehensive parametric analysis, dopant effects have been regarded analytically and numerically. Principally, through the integrated MI gain, two side bands of MI were detected, and one debated on their relationship with the pyramidal form of the maximum gain for the odd order dispersion coefficients. Coupled to the bifurcation theory, numerical investigations of our analytical predictions have led to their satisfactory confirmation, via the generation of several solitons with different energies at the same distance.

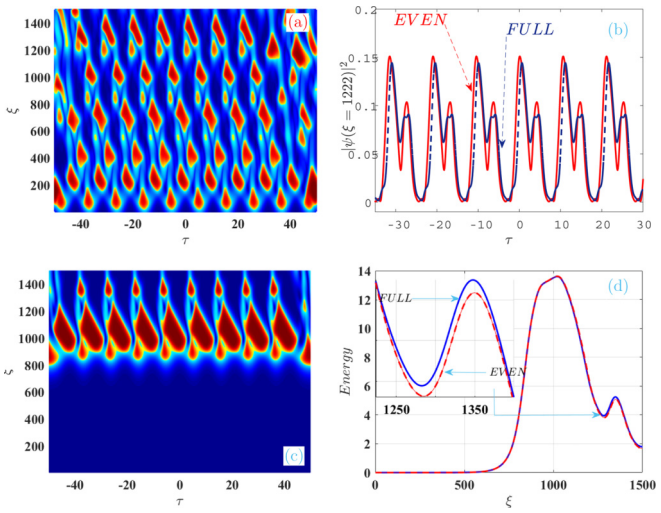

FIG. 23. Numerical evolution $[\xi(m), \tau(ps)]$ of the modulational instability in the full model: (a) Propagation of the CW when $P_0 = 1$. (b) Transverse distributions of the intensity at position $\xi = 1222m$, considering full dispersion (solid line) and even dispersion (dashed line). (c) Propagation when $P_0 = 1.5$. (d) Energy with full dispersion (solid line) and even dispersion (dashed line). Parameters are the same as in Fig. 21.

While the odd dispersion coefficients were found to reduce the intensity of the continuous wave, the even dispersion coefficients, for their part, supported the appearance of several regions of instability through the integrated MI gain, the main consequence being an increase of the maximum gain due to nonlinearity gradients and their corresponding correction terms. Other indicators like the center of mass also opened a new route to some excellent physical features of MI that will be useful in future studies devoted to the nonlinear manifestation of MI. To conclude, the procedure adopted here can be employed to investigate other signatures of MI such as chaotic dynamics of solitons, which reinforces the universality of bifurcation theory and makes it more effective and very attractive, especially in dissipative systems.

ACKNOWLEDGMENTS

We thank the anonymous reviewers for their thorough review and invaluable comments, which improved this paper significantly.

APPENDIX

Here, we have the coefficients A_n of the solution Eq. (9)

$$A_{12} = {d_{6r}}^2, \tag{A1}$$

$$A_{11} = 2d_{5r}d_{6r}, \tag{A2}$$

$$A_{10} = -\left(2d_{4r}d_{6r} + {d_{5r}}^2\right), \tag{A3}$$

$$A_9 = -2(d_{4r}d_{5r} + d_{3r}d_{6r}), \tag{A4}$$

$$A_8 = 2(d_{5r}d_{3r} + d_{2r}d_{6r}) + {d_{4r}}^2, \tag{A5}$$

$$A_7 = 2(d_{4r}d_{3r} + d_{5r}d_{2r}) + 2d_{6r}m_{1r}P_0A_\xi^2 + 4d_{6r}m_{2r}{P_0}^2A_\xi^4 + 6d_{6r}m_{3r}{P_0}^3A_\xi^6, \tag{A6}$$

$$A_6 = -2d_{2r}d_{4r} - {d_{3r}}^2 - 2P_0(d_{6r}d_{2r} + d_{5r}m_{1r})A_\xi^2 - 4{P_0}^2(d_{5r}m_{2r} + d_{6r}q_{2r})A_\xi^4 - 6{P_0}^3(d_{6r}q_{3r} + d_{5r}m_{3r})A_\xi^6, \tag{A7}$$

$$A_5 = -2d_{2r}d_{3r} - 2P_0(d_{4r}m_{1r} + d_{5r}q_{1r})A_\xi^2 - 4{P_0}^2(d_{4r}m_{2r} + d_{5r}q_{2r})A_\xi^2, \tag{A8}$$

$$A_4 = {d_{2r}}^2 + 2P_0(d_{4r}q_{1r} + d_{3r}m_{1r})A_\xi^2 + 4{P_0}^2(d_{4r}q_{1r} + d_{3r}m_{2r})A_\xi^4 + 6{P_0}^3(d_{4r}q_{3r} + d_{3r}m_{3r})A_\xi^6, \tag{A9}$$

$$A_3 = 2P_0(d_{3r}q_{1r} + d_{2r}m_{1r})A_\xi^2 + 4{P_0}^2(d_{3r}d_{4r} + d_{2r}m_{2r})A_\xi^4 + 6{P_0}^3(d_{2r}m_{3r} + d_{3r}q_{3r})A_\xi^6, \tag{A10}$$

$$A_2 = 9{P_0}^6{n_{3s}}^2A_\xi^{12} + 12{P_0}^5n_{3s}n_{2s}A_\xi^{10} + 2{P_0}^4\left(2{n_{2s}}^2 + 3n_{1s}n_{3s}\right)A_\xi^8 + 2{P_0}^3(2n_{1s}n_{2s} - 3q_{3r}q_{3r})A_\xi^6 + {P_0}^2\left({n_{1s}}^2 - 4d_{2r}q_{2r}\right)A_\xi^4 - 2A_\xi^2d_{2r}q_{1r}P_0, \tag{A11}$$

$$A_1 = 2{P_0}^3q_{2s}n_{1s}A_\xi^6 + 4{P_0}^4(n_{2s}q_{3s} + 2q_{3s}n_{1s})A_\xi^8 + 2{P_0}^5(3q_{2s}n_{3s} + 4q_{3s}n_{2s})A_\xi^{10} + 12{P_0}^6q_{3s}n_{3s}A_\xi^{12}, \tag{A12}$$

$$A_0 = -{P_0}^4\left({q_{2s}}^2A_\xi^8 + 4q_{3s}P_0A_\xi^{10}q_{2s} + 4{q_{3s}}^2{P_0}^2A_\xi^{12}\right). \tag{A13}$$

The coefficients of the frequency detuning in the full model defined in Eq. (16) are

$$C_0 = \frac{{d_{4s}}^3}{27{d_{6s}}^3} - \frac{d_{2s}d_{4s}}{6{d_{6s}}^2} + \frac{{P_0}^2A_\xi^4(2q_{3s}P_0A_\xi^2 + q_{3s})}{2d_{6s}}, \tag{A14}$$

$$C_1 = \left(81(\Xi)^2 + 12\left(\frac{d_{2s}}{d_{6s}} - \frac{{d_{4s}}^2}{3{d_{6s}}^2}\right)^3\right)^{1/2}, \tag{A15}$$

where

$$\Xi = -\frac{2{d_{4s}}^3}{27{d_{6s}}^3} + \frac{d_{2s}d_{4s}}{3{d_{6s}}^2} - \frac{{P_0}^2A_\xi^4(2\,q_{3s}P_0A_\xi^2 + q_{2s})}{d_{6s}}. \tag{A16}$$

The correction term of the Lange-Newell criterion defined in Eq. (18) is

$$Y_{11} = -\frac{{d_{6s}}^2\Omega^{10}}{2P_0} + \frac{(2d_{6s}d_{4s} - 2d_{4r}d_{6r})\Omega^8}{2P_0} + \frac{\left(-2d_{2s}d_{6s} + 2d_{2r}d_{6r} - 2d_{3s}d_{5s} - {d_{4s}}^2\right)\Omega^6}{2P_0} + \frac{\left(2P_0q_{1s}d_{6s} + 4P_0^2q_{2s}d_{6s} - 4d_{6r}P_0^2q_{2r}\right)\Omega^4}{2P_0} + \frac{\left(6n_{s2}P_0^2d_{5s} + 4n_{1s}P_0d_{5s} + 8d_{5s}n_{3s}P_0^3\right)\Omega^4}{2P_0} + \frac{\left(-2d_{6r}P_0q_{1r} - 2d_{4\,r}d_{2r} + 2d_{2s}d_{4s}\right)\Omega^4}{2P_0}$$

$$+\frac{\left(-8d_{3s}n_{3s}P_0^3+2d_{4r}P_0q_{1r}-4d_{3s}n_{1s}\right)\Omega^2}{2P_0}$$
$$+\frac{\left(6\,d_{4r}P_0^3q_{3r}-6P_0^3q_{3s}d_{4s}\right)\Omega^2}{2P_0}$$
$$+\frac{\left(-2P_0q_sd_{4s}-6d_{3s}n_{2s}P_0^2\right)\Omega^2}{2P_0}$$
$$+\frac{\left(6d_{4r}P_0^3q_{3r}-6P_0^3q_{3s}d_{4s}-{d_{2s}}^2\right)\Omega^2}{2P_0}$$
$$+2P_0q_{2s}d_{2s}+\frac{5}{2}{n_{1s}}^2P_0+18n_{2s}P_0^4n_{3s}$$
$$+3P_0^2q_{3s}d_{2s}+11n_{1s}P_0^3n_{3s}$$
$$+8n_{2s}P_0^2n_{1s}-3d_{2r}P_0^2q_{3r}-2d_{2\,r}P_0q_{2r}. \tag{A17}$$

[1] M. Peyrard and T. Dauxois, *Physique des Solitons* (EDP Sciences, CNRS Édition, Paris, 2004).

[2] Y. S. Kivshar and G. P. Agrawal, *Optical Solitons: From Fibers to Photonic Crystals* (Academic Press, San Diego, 2003).

[3] N. Akhmediev and A. Ankiewicz, *Dissipative Solitons* (Springer, Berlin, 2005).

[4] N. Akhmediev and A. Ankiewicz, *Dissipative Solitons: From Optics to Biology and Medicine*, Lecture Notes in Physics, Vol. 751 (Springer, Berlin, Heidelberg, 2008).

[5] A. Hasegawa, An historical review of application of optical solitons for high speed communications, Chaos **10**, 475 (2000).

[6] W. Chang, A. Ankiewicz, and N. Akhmediev, Creeping solitons in dissipative systems and their bifurcations, Phys. Rev. E **76**, 016607 (2007).

[7] J. M. Soto-Crespo, M. Grapinet, P. Grelu, and N. Akhmediev, Bifurcations and multiple-period soliton pulsations in a passively mode-locked fiber, Phys. Rev. E **70**, 066612 (2004).

[8] P. Grelu and N. Akhmediev, Dissipative solitons for mode-locked lasers, Nat. Photon. **6**, 84 (2012).

[9] N. Akhmediev, J. M. Soto-Crespo, and G. Town, Pulsating solitons, chaotic solitons, period doubling, and pulse coexistence in mode-locked lasers: Complex Ginzburg-Landau equation approach, Phys. Rev. E **63**, 056602 (2001).

[10] J. M. Soto-Crespo, N. Akhmediev, and A. Ankiewicz, Pulsating, Creeping, and Erupting Solitons in Dissipative Systems, Phys. Rev. Lett. **85**, 2937 (2000).

[11] W. Chang, J. M. Soto-Crespo, P. Vouzas, and N. Akhmediev, Extreme soliton pulsations in dissipative systems, Phys. Rev. E **92**, 022926 (2015).

[12] N. Akhmediev, J. M. Soto-Crespo, P. Vouzas, N. Devine, and W. Chang, Dissipative solitons with extreme spikes in the normal and anomalous dispersion regimes, Philos. Trans. R. Soc. A Math. Phys. Eng. Sci. **376**, 20180023 (2018).

[13] M. I. Carvalho and M. Facão, Dissipative solitons for generalizations of the cubic complex Ginzburg-Landau equation, Phys. Rev. E **100**, 032222 (2019).

[14] M. I. Carvalho and M. Facão, Plain and oscillatory solitons of the cubic complex Ginzburg-Landau equation with nonlinear gradient terms, Phys. Rev. E **96**, 042220 (2017).

[15] M. I. Carvalho and M. Facão, Existence and stability of solutions of the cubic complex Ginzburg-Landau equation with delayed Raman scattering, Phys. Rev. E **92**, 022922 (2015).

[16] G. P. Agrawal, Optical pulse propagation in doped fiber amplifiers, Phys. Rev. A **44**, 7493 (1991).

[17] G. P. Agrawal, *Applications of Nonlinear Fiber Optics* (Academic press, San Diego, 2001).

[18] X. Feng, Y. Liu, S. Fu, S. Yuan, and X. Dong, Switchable dual-wavelength ytterbium-doped fiber laser based on a few-mode fiber grating, IEEE Photon. Technol. Lett. **16**, 3 (2004).

[19] Y. E. Jeong, J. K. Sahu, D. N. Payne, and J. Nilsson, Ytterbium-doped large-core fiber laser with 1.36 kW continuous-wave output power, Opt. Exp. **12**, 6088 (2004).

[20] L. M. Zhao, D. Y. Tang, H. Zhang, X. Wu, Q. Bao, and K. P. Loh, Dissipative soliton operation of an ytterbium-doped fiber laser mode locked with atomic multilayer graphene, Opt. Lett. **35**, 3622 (2010).

[21] M. Zhang, E. J. R. Kelleher, F. Torrisi, Z. Sun, T. Hasan, D. Popa, F. Wang, A. C. Ferrari, S. V. Popov, and J. R. Taylor, Tm-doped fiber laser mode-locked by graphene-polymer composite, Opt. Express **20**, 25077 (2012).

[22] Z. Luo, M. Zhou, J. Weng, G. Huang, H. Xu, C. Ye, and Z. Cai, Graphene-based passively Q-switched dual-wavelength Erbium-doped fiber laser, Opt. Lett. **35**, 3709 (2010).

[23] Y. Chen, C. Zhao, S. Chen, J. Du, P. Tang, G. Jiang, H. Zhang, S. Wen, and D. Tang, Large energy, wavelength widely tunable, topological insulator Q-switched erbium-doped fiber laser, IEEE J. Sel. Top. Quantum Electron. **20**, 0900508 (2013).

[24] H. Zhang, D. Y. Tang, L. M. Zhao, Q. L. Bao, and K. P. Loh, Large energy mode locking of an erbium-doped fiber laser with atomic layer graphene, Opt. Express **17**, 17630 (2009).

[25] F. Sanchez, P. le Boudec, P. L. François, and G. Stephan, Effects of ion pairs on the dynamics of erbium-doped fiber laser, Phys. Rev. A **48**, 2220 (1993).

[26] L. Luo, T. J. Tee, and P. L. Chu, Chaotic behavior in erbium-doped fiber-ring lasers, J. Opt. Soc. Am. B **15**, 972 (1998).

[27] S. Gatz and J. Herrmann, Soliton propagation and soliton collision in double-doped fibers with a non-Kerr-like nonlinear refractive-index change, Opt. Lett. **17**, 484 (1992).

[28] Y.-F. Chen, K. Beckwitt, F. W. Wise, B. G. Aitken, J. S. Sanghera, and I. D. Aggarwal, Measurement of fifth- and seventh-order nonlinearities of glasses, J. Opt. Soc. Am. B **23**, 347 (2006).

[29] A. Mohamadou, C. G. Latchio Tiofack, and T. C. Kofané, Wave train generation of solitons in systems with higher-order nonlinearities, Phys. Rev. E **82**, 016601 (2010).

[30] M. Djoko and T. C. Kofané, Dissipative optical bullets modeled by the cubic-quintic-septic complex Ginzburg-Landau equation with higher-order dispersions, Commun. Nonlinear Sci. Numer. Simulat. **48**, 179 (2017).

[31] M. Djoko and T. C. Kofané, The cubic-quintic-septic complex Ginzburg-Landau equation formulation of optical pulse propagation in 3D doped Kerr media with higher-order dispersions, Opt. Commun. **416**, 190 (2018).

[32] M. Djoko and T. C. Kofané, Dissipative light bullets: from stationary light bullets to double, quadruple, six-fold, eight-fold,

and ten-fold bullet complexes, Commun. Nonlinear Sci. Numer. Simulat. **68**, 169 (2019).

[33] M. Djoko, C. B. Tabi, and T. C. Kofané, Robust propagation of optical vortex beams, necklace-ring solitons, soliton clusters, and uniform-ring beams generated in the frame of the higher-order (3+1)-dimensional cubic-quintic-septic complex Ginzburg-Landau equation, Phys. Scr. **94**, 075501 (2019).

[34] S. I. Fewo, C. M. Ngabireng, and T. C. Kofané, Ultrashort optical solitons in the cubic-quintic complex Ginzburg-Landau equation with higher-order terms, Phys. Soc. Jpn. **77**, 074401 (2008).

[35] S. I. Fewo and T. C. Kofané, A collective variable approach for optical solitons in the cubic-quintic complex Ginzburg-Landau equation with third-order dispersion, Opt. Commun. **281**, 2893 (2007).

[36] K. Porsezian, K. Nithyanandan, R. V. J. Raja, and P. K. Shukla, Modulational instability at the proximity of zero dispersion wavelength in the relaxing saturable nonlinear system, J. Opt. Soc. Am. B **29**, 2803 (2012).

[37] R. V. J. Raja, K. Porsezian, and K. Nithyanandan, Modulational-instability-induced supercontinuum generation with saturable nonlinear response, Phys. Rev. A **82**, 013825 (2010).

[38] P. Tchofo Dinda, C. M. Ngabireng, K. Porsezian, and B. Kalithasan, Modulational instability in optical fibers with arbitrary higher-order dispersion and delayed Raman response, Opt. Commun. **266**, 142 (2006).

[39] K. Nithyanandan, R. V. J. Raja, K. Porsezian, and B. Kalithasan, Modulational instability with higher-order dispersion and walk-off in Kerr media with cross-phase modulation, Phys. Rev. A **86**, 023827 (2012).

[40] J. T. Kippenberg, A. L. Gaeta, M. Lipson, and M. L. Gorodetsky, Dissipative Kerr solitons in optical microresonators, Science **361**, 8083 (2018).

[41] R. Murali and K. Porsezian, Modulational instability and moving gap soliton in Bose-Einstein condensation with Feshbach resonance management, Phys. D (Amsterdam, Neth.) **239**, 1 (2010).

[42] T. S. Raju, P. K. Panigrahi, and K. Porsezian, Modulational instability of two-component Bose-Einstein condensates in a quasi-one-dimensional geometry, Phys. Rev. A **71**, 035601 (2005).

[43] T. Mithun and K. Porsezian, Modulational instability of $F = 2$ spinor condensates, Phys. Rev. A **85**, 013616 (2012).

[44] E. Wamba, A. Mouhamadou, and T. C. Kofané, Modulational instability of a trapped Bose-Einstein condensate with two and three-body interactions, Phys. Rev. E **77**, 046216 (2008).

[45] N. Kumar, A. Pukhov, and K. Lotov, Self-Modulation Instability of a Long Proton Bunch in Plasmas, Phys. Rev. Lett. **104**, 255003 (2010).

[46] C. S. Panguetna, C. B. Tabi, and T. C. Kofané, Electronegative nonlinear oscillating modes in plasmas, Commun. Nonlinear Sci. Numer. Simulat. **55**, 326 (2018).

[47] C. S. Panguetna, C. B. Tabi, and T. C. Kofané, Two-dimensional modulated ion-acoustic excitation in electronegative plasmas, Phys. Plasmas **24**, 092114 (2017).

[48] A. Hasegawa, *Plasma Instabilities and Nonlinear Effects* (Springer-Verlag, Heidelberg, 1975).

[49] C. K. W. Tam, Amplitude dispersion and nonlinear instability of whistlers, Phys. Fluids **12**, 1028 (1969).

[50] T. Taniuti and H. Washimi, Self-Trapping and Instability of Hydromagnetic Waves Along the Magnetic Field in a Cold Plasma, Phys. Rev. Lett. **21**, 209 (1968).

[51] I. Maïna, C. B. Tabi, A. Mohamadou, H. P. F. Ekobena, and T. C. Kofané, Discrete impulses in ephaptically coupled nerve fibers, Chaos **25**, 043118 (2015).

[52] C. B. Tabi, I. Maïna, A. Mohamadou, H. P. F. Ekobena, and T. C. Kofané, Long-range intercellular Ca^{2+} wave patterns, Phys. A (Amsterdam, Neth.) **435**, 1 (2015).

[53] A. K. S. Ali, K. Nithyanandan, K. Porsezian, and A. I. Maimistov, Modulation instability in a triangular three-core coupler with a negative-index material channel, J. Opt. **18**, 035102 (2016).

[54] W. Krolikowski, O. Bang, J. J. Rasmussen, and J. Wyller, Modulational instability in nonlocal nonlinear Kerr media, Phys. Rev. E **64**, 016612 (2001).

[55] D. Zanga, S. I. Fewo, C. B. Tabi, and T. C. Kofané, Modulational instability in weak nonlocal nonlinear media with competing Kerr and non-Kerr nonlinearities, Commun. Nonlinear Sci. Numer. Simulat. **80**, 104993 (2020).

[56] B. K. Esbensen, A. Wlotzka, M. Bache, O. Bang, and W. Krolikowski, Modulational instability and solitons in nonlocal media with competing nonlinearities, Phys. Rev. A **84**, 053854 (2011).

[57] R. Ganapathy, K. Senthilnathan, and K. Porsezian, Modulational instability in a fibre and a fibre Bragg grating, J. Opt. B **6**, S436 (2004).

[58] K. Porsezian and K. Senthilnathan, Generation of Bragg solitons through modulation instability in a Bragg grating structure, Chaos **15**, 037109 (2005).

[59] J. Ancemma, K. Senthilnathan, K. Porsezian, and P. Tchofo Dinda, Gap solitons and modulation instability in a dynamic Bragg grating with nonlinearity management, J. Opt. A **11**, 015203 (2009).

[60] K. Porsezian, K. Senthilnathan, and S. Devipriya, Modulational Instability in fiber Bragg grating with non-Kerr Nonlinearity, IEEE J. Quantum Electron. **41**, 789 (2005).

[61] K. Nithyanandan, R. V. J. Raja, and K. Porsezian, Modulational instability in a twin-core fiber with the effect of saturable nonlinear response and coupling coefficient dispersion, Phys. Rev. A **87**, 043805 (2013).

[62] R. Ganapathy, B. A. Malomed, and K. Porsezian, Modulational instability and generation of pulse trains in asymmetric dual-core nonlinear optical fibers, Phys. Lett. A **354**, 366 (2006).

[63] R. Haldar, A. Roy, P. Mondal, V. Mishra, and S. K. Varshney, Free-carrier-driven Kerr frequency comb in optical microcavities: Steady state, bistability, self-pulsation, and modulation instability, Phys. Rev. A **99**, 033848 (2019).

[64] K. Nithyanandan, R. V. J. Raja, and K. Porsezian, Theoretical investigation of modulational instability in semiconductor doped dispersion decreasing fiber and its cutting edge over the existing fiber systems, J. Opt. Soc. Am. B **30**, 178 (2013).

[65] G. P. Agrawal, Modulation instability in erbium-doped fiber amplifiers, IEEE Photon. Technol. Lett. **4**, 562 (1992).

[66] S. V. Gurevich, C. Schelte, and J. Javaloyes, Impact of high-order effects on soliton explosions in the complex cubic-quintic Ginzburg-Landau equation, Phys. Rev. A **99**, 061803(R) (2019).

[67] J. M. Soto-Crespo and N. Akhmediev, Soliton as Strange Attractor: Nonlinear Synchronization and Chaos, Phys. Rev. Lett. **95**, 024101 (2005).

[68] K. K. Ndebele, C. B. Tabi, and T. C. Kofané, Modulational instability in nonlinear doped optical fiber induced by the cubic-quintic-septic complex Ginzburg-Landau equation with higher-order dispersions, J. Opt. Soc. Am. B **37**, A214 (2020).

[69] C. G. Latchio Tiofack, A. Mohamadou, T. C. Kofané, and A. B. Moubissi, Generation of pulse trains in nonlinear optical fibers through the generalized complex Ginzburg-Landau equation, Phys. Rev. E **80**, 066604 (2009).

[70] C. G. Lange and A. C. Newell, A stability criterion for envelope equation, Siam J. Appl. Math. **27**, 441 (1974).

[71] F. II. Ndzana, A. Mohamadou, and T. C. Kofané, Discrete Lange-Newell criterion for dissipative systems, Phys. Rev. E **79**, 056611 (2009).

[72] F. B. Pelap and T. C. Kofané, Modulation instability in some physical systems, Phys. Scr. **64**, 410 (2001).

[73] A. Mohamadou, B. E. Ayissi, and T. C. Kofané, Instability criteria and pattern formation in the complex Ginzburg-Landau equation with higher-order terms, Phys. Rev. E **74**, 046604 (2006).

[74] S. Marino, I. B. Hogue, C. J. Ray, and D. E. Kirschner, A methodology for performing global uncertainty and sensitivity analysis in systems biology, J. Theor. Biol. **254**, 178 (2009).

[75] S. A. Pedro, H. E. Z. Tonnang, and S. Abelman, Uncertainty and sensitivity analysis of a Rift Valley fever model, Comput. Math. Appl **279**, 170 (2016).

[76] M. M. Foudjio, F. T. Ndjomatchoua, C. L. Gninzanlong, and C. Tchawoua, Collective escape and supratransmission phenomena in a nonlinear oscillators chain, Chaos **30**, 123122 (2020).

[77] B. S. Djouda, F. T. Ndjomatchoua, F. M. Moukam Kakmeni, C. Tchawoua, and H. E. Z. Tonnang, Understanding biological control with entomopathogenic fungi: Insights from a stochastic pest-pathogen model, Chaos **31**, 023126 (2021).

[78] A. K. S. Ali, K. Porsezian, and T. Uthayakumar, Influence of self-steepening and intrapulse Raman scattering on modulation instability in oppositely directed coupler, Phys. Rev. E **90**, 042910 (2014).